A computational study of CaWO4: Raman spectrum, intrinsic defects, and excited state properties

Tanguy Ferré, Théo Cavignac, Stéphane Jobic, Camille Latouche

A computational study of $CaWO_4$: Raman spectrum, intrinsic defects, and excited state properties

Tanguy Ferré, Théo Cavignac, Stéphane Jobic, Camille Latouche*
Nantes Université, CNRS, Institut des Matériaux de Nantes Jean Rouxel, IMN, F-44000 Nantes, France
camille.latouche@cnrs-imn.fr

Abstract

In this study, we present an ab initio investigation of the optical properties of $CaWO_4$. The crystal structure of the bulk material along with its vibrational (in the ground state) and optical properties (in both ground and excited states) were analyzed. Our simulations accurately identified the observed Raman signature of the material. Additionally, we simulated the intrinsic luminescence properties of $CaWO_4$ and identified the charge transfer that occurs during the de-excitation process. Finally, through the use of *ab initio* techniques, the intrinsic defect formation energies and their corresponding concentrations were determined providing the first instance of such findings for this material.

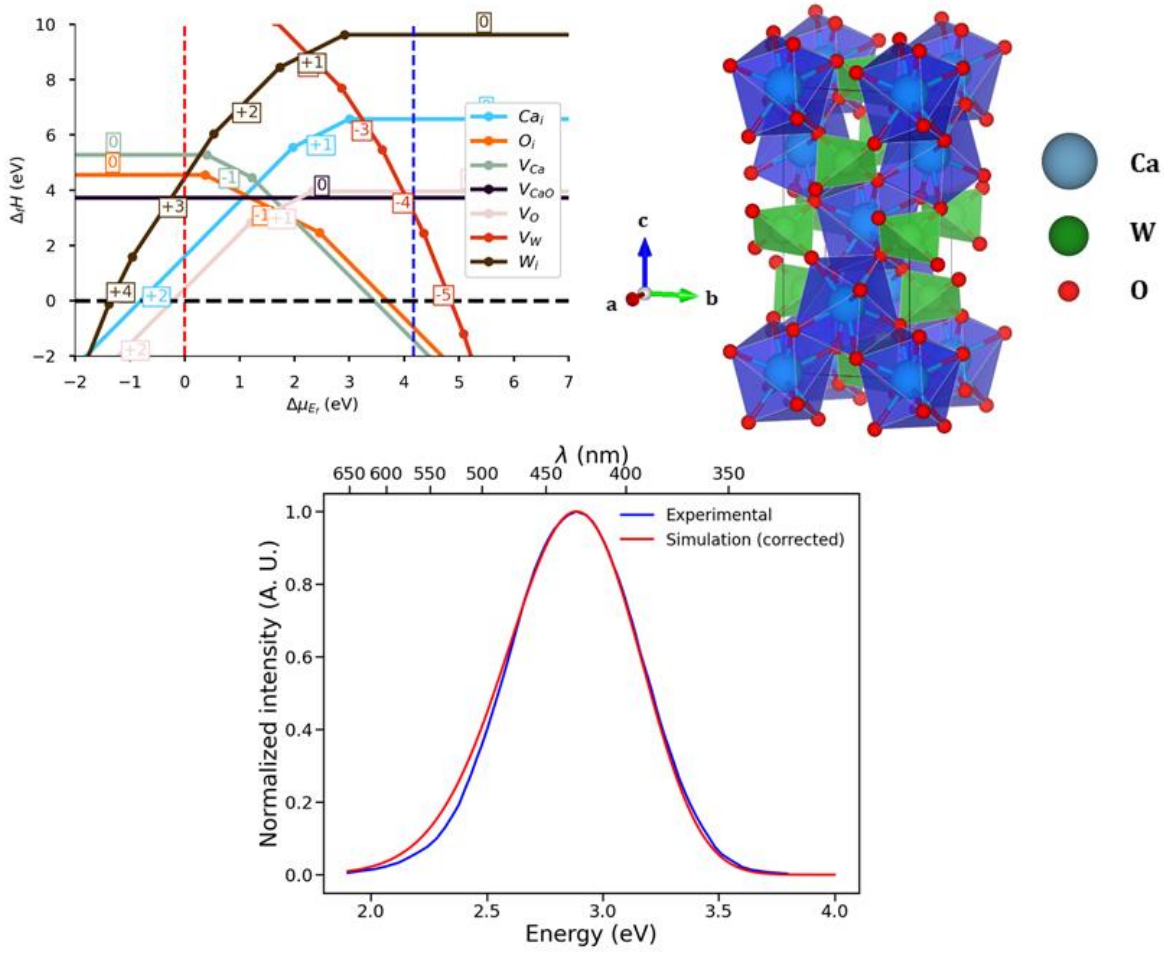

INTRODUCTION

Calcium tungstate, hereafter labelled $CaWO_4$, is commonly found in its mineral form, namely the scheelite. For decades, this material has been studied due to its remarkable ability to emit a strong blue light in the visible spectrum,[1–3] under short wave UV radiation.[4,5,6] Its first applications date back to the end of the 19th century, when it was used in radiography taking advantage of its light emission under X-ray irradiation.[5,6] Since then, it has found interesting applications as a phosphor,[7] scintillator,[8,9] and even as an active laser medium.[10] However, the challenge remains to use this material in devices such as lasers or optical fibers.[11] To achieve that, researchers are exploring numerous ways to optimize the properties of calcium tungstate.[12,13] Recent researches have focused on optimizing the material's luminescence properties through doping with various rare earth ions or transition metals.[9] Another area of focus is on improving the growth techniques of $CaWO_4$ syntheses by controlling their size and shape through adjustments to the synthesis process conditions.[13]

Experimentalists have explored multiple synthesis pathways, such as the microwave route,[14] micro emulsion,[15] molten salt,[16] or auto ignition combustion.[17] These numerous attempts allowed the characterization of many spectroscopic properties of the material. For instance, its vibrational properties were reported while its luminescence properties have been the subject of numerous theories.[18,19] Among these theories, the question concerning the mechanism responsible for such properties is a central topic of discussion.[11,20–25]

As an example, some authors stated that the blue luminescence is arising from an electronic transition of charge transfer type within the WO_4^{2-} tetrahedra,[2] whereas others assigned it to it to self-trapped electron states.[26] Indeed, as is often the case with such materials, defects can significantly affect the observed properties. In the case of calcium tungstate, many studies have shown that defects can dramatically modify the material's properties.[11,20–24,27,28]

Concretely, numerous articles have already dealt with the photoluminescence of such material concerning the blue emission band peaking at 420 nm, despite a strong convergence toward the implication of the WO_4 tetrahedra.[2,4,5,8,11,18,22,26,29] In the same manner, the recorded band gap is also quite controversial.[21,22,30–33] Very surprisingly, despite the large number of experimental studies, there are only few theoretical and computational studies on this material reporting on the electronic properties.[21,34,35] Furthermore, there have been no reports on a systematic investigation of the intrinsic defects of $CaWO_4$, nor have the luminescence properties been properly simulated.

To fill this gap, an *ab initio* study on this material has been started, dealing with the vibrational and the optical properties alongside the impact of intrinsic defects.

The first focus was on the description of its crystallographic structure, presented in Figure 1, to enhance the link with its properties.

The agreement between our simulations and the experimental parameters related to the material's optical properties, including its absorption and emission properties, as well as its refractive index, are discussed. Additionally, a discussion on the intrinsic defects of $CaWO_4$ and their propensity to form is provided.

Computational details

Electronic computations and the defect studies were performed using the Vienna Ab initio Simulation Package (VASP)[36–39] and the Perdew-Burke-Ernzerhof (PBE) functional with +U Hubbard term (except if mentioned). The Projector Augmented Wave (PAW) method was employed with a cutoff energy set to 540 eV.

The impact of the Hubbard term on the "d" electrons of tungsten has also been considered, and is discussed in the next part. Different values of U were tested ranging from zero to six. For a U value equals to three, both the structure and the bandgap were efficiently reproduced.

While the structural and optical properties were computed on the conventional cell, calculations for the defect study and the investigation of luminescence properties (using constrained-DFT, hereafter labelled CDFT)[40] were performed on a 2x2x1 supercell containing 96 atoms. For the supercell calculations, the planewave energy cutoff was set to 540 eV. A k-mesh of 3x3x3 for the structural optimization and single point energy calculations was used. All computations were performed with spin-polarization.

In such a situation, defect formation energies (DFE) were calculated considering the following formula (equation 1):

$$(1)\quad \Delta_f H^{D,q}(\mu_{E_F}) = E_{tot}^{D,q} - E_{tot}^{host} + \sum_i n_i\mu_i + q\left(E_{VBM}^{host} + \Delta\mu_{E_F}\right) + E_{corr}(D,q)$$

where $\Delta_f H^{D,q}$ is the formation enthalpy of a defect D in a state of charge q, $E_{tot}^{D,q}$ is the total energy of the faulted supercell, E_{tot}^{host} is the total energy of the host supercell, n_i is the number of atoms of the i^{th} species added ($n_i < 0$) or removed ($n_i > 0$) from the ideal probed material, μ_i is the chemical potential of the i^{th} species, μ_{E_F} is the chemical potential of the electronic reservoir relative to E_{VBM}^{host}, the energy of the valence band maximum (VBM) of the host. E_{corr} corresponds to various corrections of spurious effects, such as electrostatic interactions between point defects or the potential alignment allowing to retrieve the electronic reference of the host material. The chemical potential μ_i corresponds to the atomic reservoir of the i^{th} atomic species during the crystal growth. Obviously, this quantity strongly depends on the synthesis conditions and drives the thermodynamic stability between the different competitive phases. For a given i^{th} atomic species, the chemical potential μ_i may be decomposed as the sum of the standard chemical potential μ_i^0 and the deviation $\Delta\mu_i$ which depends on synthesis conditions. All these computations of other phases were performed with the VASP software. In the case of a finite cell used to simulate a charged system, the electrostatic potential is shifted by an undetermined value. The Potential Alignment (PA) correction allows to adjust the charged cell energies by averaging the difference between the potential felt by an atom far from the defect $V_{D,q}^r$ and the potential in the ideal cell V_{host}^r. It is formulated as equations 2 and 3:

$$(2)\quad \Delta V = \left(V_{D,q}^r - V_{host}^r\right)$$

$$(3)\quad \Delta E_{PA} = q \times \overline{\Delta V}$$

The size of the supercells is drastically limited by the computational cost, which induces high concentrations of defects. In such a situation, Moss-Burstein band-filling effects exist when electrons or holes relax to PHS, respectively.[41,42] To remove this band-filling effects, the Moss-Burstein (MB) correction has to be taken into account. It expresses as (equation 4):

$$(4)\quad \begin{cases} \Delta E_{MB}^{e^-} &= -\sum^{n,k} \omega_k \eta_{n,k}\left(\epsilon_{n,k} - \left[E_C^{host} + \overline{\Delta V}\right]\right)\cdot\Theta\left(\epsilon_{n,k} - \left[E_C^{host} + \overline{\Delta V}\right]\right) \\ \Delta E_{MB}^{h^+} &= -\sum_{n,k} \omega_k\left(2 - \eta_{n,k}\right)\left(\left[E_V^{host} + \overline{\Delta V}\right] - \epsilon_{n,k}\right)\cdot\Theta\left(\left[E_V^{host} + \overline{\Delta V}\right] - \epsilon_{n,k}\right) \end{cases}$$

where ω_k is the weight of k-point k, $\eta_{n,k}$ is the occupation of band n for k-point k, $\epsilon_{n,k}$ is the energy of band n for k-point k, and Θ is the Heaviside function.

In the supercell model, the point defect may interact electrostatically with its periodic images.[43] Such effects are removed using the Makov-Payne (MP) correction formulated by Zunger and coworkers[44–46] as equation 5:

$$(5) \quad \Delta E_{MP} = \left(1 + c_{sh}(1 - \epsilon^{-1})\right)\frac{q^2 \alpha_M}{2\epsilon\Omega^{1/3}}$$

where c_{sh} is a geometry dependent correction term, ϵ is the dielectric constant of the material, α_M is the Madelung constant and Ω the volume. The total dielectric constant (i.e. ionic + optical dielectric constant) was computed using both the VASP (11.65) and Crystal (9.55) packages, using the PBE+U and PBE approximations, respectively. The obtained values are in good agreement with respect to available experimental data (10.56 ± 0.4 and 10.96 ± 0.13).[47,48]

The charge transition level $\epsilon(q/q')$ between two charge states q and q' corresponds to the μ_{E_F} level at which their respective DFEs are equivalent, *i.e.,* the populations of both q and q' states are identical within the material for this specific potential. Such thermodynamic quantity is expressed as equation 6:

$$(6) \quad \epsilon(q/q') = \frac{\Delta_f H^{D,q}(\mu_{E_F} = 0) - \Delta_f H^{D,q'}(\mu_{E_F} = 0)}{q' - q}$$

where $\Delta_f H^{D,q}$ and $\Delta_f H^{D,q'}$ are the formation enthalpies of a defect D in the charge states q and q', respectively.

Assuming all defects are formed during the growth process at a given temperature (T_{gr}) and their concentration maintained after quenching of the structure to room temperature, the concentration $n_{D,q}(E_F)$ of a defect D in a charge state q can be determined for a given Fermi level E_F (*i.e.,* a given temperature T since E_F depends on T) through a Fermi-Dirac distribution commonly approximated by a Boltzmann distribution for the N available sites per volume unit (equation 7):

$$(7) \quad n_{D,q}(E_F) = N \cdot exp\left(-\frac{\Delta_f H^{D,q}(E_F)}{k_B T}\right)$$

In that context, the Fermi level is determined by solving iteratively the charge neutrality equation (equation 8):

$$(8) \quad -n_e(E_F) + n_h(E_F) + \sum_D \sum_{q_i \in q_D} q_i \cdot n_{D,q_i}(E_F) = 0$$

with $n_e(E_F)$ and $n_h(E_F)$ the concentrations of free electrons in the conduction band and holes in the valence band at T, respectively. Such quantities are determined through equations 9 and 10:

$$(9) \quad n_e(E_F) = \int_{E_C}^{+\infty} g_e(E) f_{FD}(E - E_F) dE$$

and

$$(10) \quad n_h(E_F) = \int_{-\infty}^{E_V} g_h(E)\left(1 - f_{DF}(E - E_F)\right) dE$$

where f_{FD} is the Fermi-Dirac distribution (equation 11):

$$(11) \quad f_{FD}(E - E_F) = \frac{1}{1 + exp\left(\frac{E - E_F}{k_B T}\right)}$$

and $g_e(E)$ and $g_h(E)$ are the 3D density of states of electrons and holes, respectively approximated in a parabolic band model (equation 12):

$$(12) \quad g_{e,h}(E) = \frac{1}{4\pi^2}\left(\frac{2m^*_{e,h}}{\hbar^2}\right)^{\frac{3}{2}}\sqrt{E}$$

where m^*_e and m^*_h are associated to the electron and hole effective masses, respectively.

Constrained occupation of bands has been set to simulate an excited state within the CDFT framework, promoting an electron from the last occupied band of the valence band to the first empty state of the conduction band.

Vibrational properties investigations were carried out using the Crystal 17 software.[49] To do so, the PBE functional was enforced and the vibrational properties were explored with a large set of k-mesh (376 vectors in the reciprocal space).

All defect post-treatments presented above were performed using the PyDEF software.[50,51]

Results and discussion

Geometrical (bulk) properties

Experimental data indicates that $CaWO_4$ belongs to the tetragonal system, and crystallizes in the $I4_1/a$ space group (Z=4). The dimensions of the experimental conventional cell are equal to 5.24901(10) Å for the a and b parameters, and 11.3930(4) Å for the c parameter.[27] W^{6+} cations are coordinated in a tetrahedral geometry, characterized by four W-O bonds equal to 1.89 Å. The Ca^{2+} cations are bonded to eight O^{2-} split into two sets of lengths respectively equal to 2.37 and 2.40 Å. The O^{2-} anions occupy positions where their close environment is composed of two Ca atoms and one W atom.[52] In summary, $CaWO_4$ can be described as a 0D-material in which all $[WO_4]$ tetrahedra are isolated and not connected to one another.

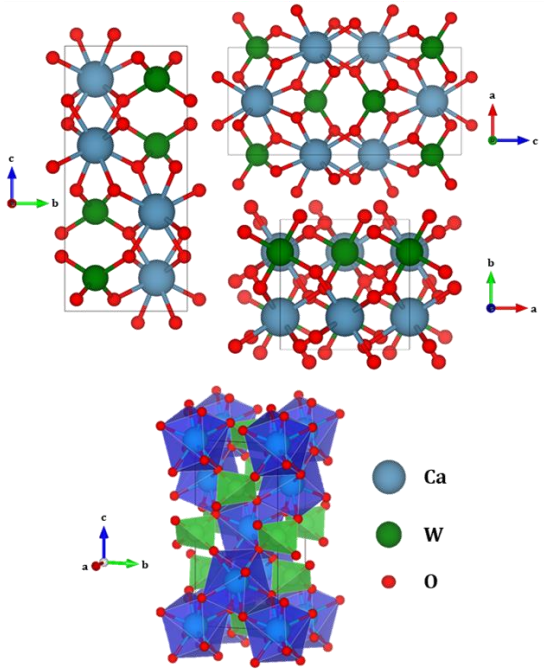

Figure 1: Crystallographic structure of $CaWO_4$. Ca, W and O correspond to the blue, green and red spheres, respectively.

The results for the structural parameters are reported in Table I. They reveal that the optimized geometry of the crystal structure is in good agreement with experimental data. The calculated cell parameters are similar to the experimental values, and the c/a ratio remains the same. While there are slight differences in the bond lengths between the experimental and calculated structures, with the calculation compressing the W-O bonds and extending the Ca-O bonds, the overall difference is small enough to be considered as a good agreement. The maximum error in bond lengths never exceeds 5%.

Table I: Experimental and calculated values of $CaWO_4$ structural parameters.

	Experimental	**Calculated** GGA + U=3
a = b (Å)	5.25	5.32
c (Å)	11.40	11.49
c/a	2.17	2.16
W-O (Å)	1.89	1.82
Ca-O "short" (Å)	2.37	2.47
Ca-O "long" (Å)	2.40	2.50

Electronic and optical (bulk) properties

As expected, the valence band is dominated by oxygen (p orbitals), while the conduction band is built upon tungsten d orbitals (see Figure 2). The computed bandgaps in PBE+U is 4.15 eV, lying in the experimental range (see Table II).[1,21,30,33] This non-underestimation of the bandgap using a classical GGA+U functional has already been reported by some of us in other oxide materials.[53]

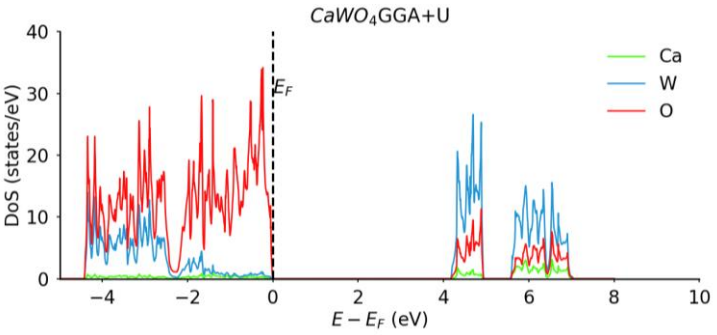

Figure 2: Calculated DOS of $CaWO_4$ (GGA+U).

Table II: Calculated and experimental values of $CaWO_4$ bandgaps and refractive indices.

	Experimental	**Calculated** GGA + U=3
Bandgap (eV)	3.87 - 5.4 [1,30,33]	4.15
Refractive index (n) (λ_{Na} = 589 nm)	1.94 [54]	1.91

As a potential incorporation into optical devices, the refractive index of $CaWO_4$ has been characterized at 1.94 at the sodium wavelength.[54,55] Our simulated value is 1.91 (see Figure 3), which is in very good agreement with the experimental one.

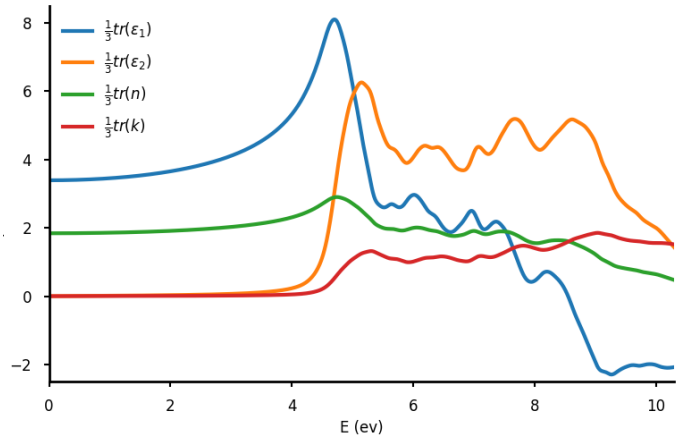

Figure 3: Optical indices of $CaWO_4$ (GGA+U): ε_1, ε_2, k and n.

Vibrational study

Herein are reported the results of the theoretical analysis performed to evaluate the vibrational properties of the studied material. As one can see in Figure 4, the agreement between the experimental and the simulated spectra is excellent in terms of energy positions, but some (slight) discrepancies appear concerning the absolute intensities. One can now assign the vibrational bands with great confidence. The most intense band located at 900 cm^{-1} corresponds to a symmetric W-O stretching motion in the A_g symmetry. At approximatively 800 and 820 cm^{-1}, two distinguishable bands of E_g and B_g symmetries can be assigned to asymmetric stretching counterpart vibrations. The slightly overestimated simulated band (in energy) at approximatively 400 cm^{-1} is a combination of B_g and E_g vibrations and is still associated to W-O nuclear motions. Furthermore, the band around 330 cm^{-1} is also associated to two vibrations (B_g and A_g) in which W-O bonds are twisting. Finally, the last band peaking at roughly 200 cm^{-1} is a combination of E_g and A_g modes, and involve all the atoms in an out-of-phase combination.

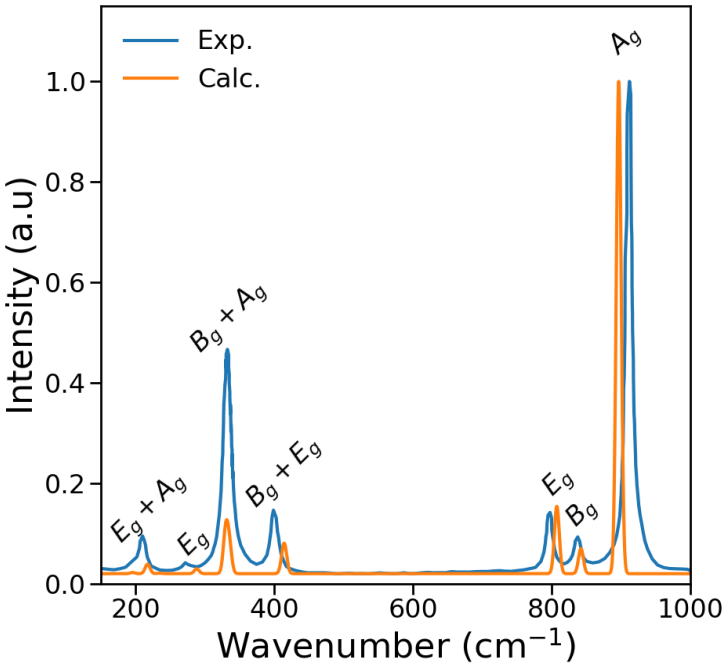

Figure 4: Experimental (blue)[18] and simulated (orange) Raman spectra of $CaWO_4$. A scale factor of 0.99 has been applied on the simulated energies with the PBE functional.

Intrinsic defects

To gain a deeper insight into the thermodynamics properties of this material, the intrinsic defects were examined by calculating their formation energies and concentrations. To begin with, the material's stability domain was determined by varying the chemical potentials of the relevant species, as illustrated in Figure 5. Three notable atmospheres were investigated because they represent the limiting conditions that may occur during the material's synthesis, namely: "A" (green dot, O–rich conditions), "B" (pink dot, W-rich/O-poor conditions) and "C" (yellow dot, averaged conditions) where the chemical potentials are uniformly distributed. Based on these findings, the limiting conditions were determined.

Table III gathers the values corresponding to the defined points of the $CaWO_4$ stability diagram.

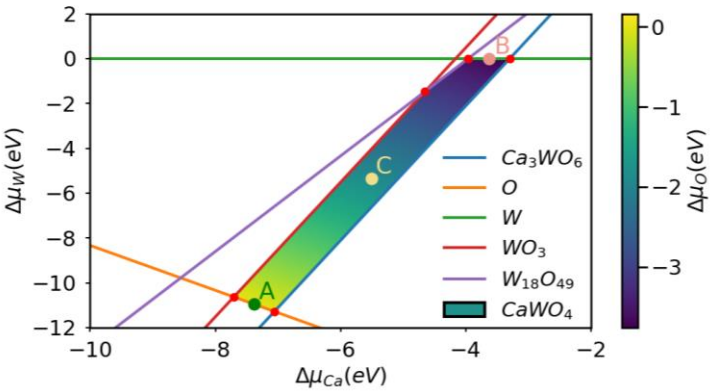

Figure 5: Stability domain of $CaWO_4$ and its competing phases. For the sake of clarity, only the phases bordering the stability domain are represented. In addition to them, CaO_2, CaO, Ca and W_8O_{21} were considered.

Table III: Limit values of the chemical potentials from the stability domain of $CaWO_4$.

Atmosphere	$\Delta\mu_{Ca}$ (eV)	$\Delta\mu_W$ (eV)	$\Delta\mu_O$ (eV)
(A)	-7.38	-10.96	0.00
(B)	-3.63	0.00	-3.68
(C)	-5.50	-5.35	-1.85

The DFE curves plotted against the Fermi energy for the respective atmospheres, along with the charge transition levels, are given in Figure 6.

The analysis of the DFE for $CaWO_4$ reveals the global trends in the intrinsic defect formation process among various chemical environments. The first trend is observed in atmospheres that are O-rich/W-poor/Ca-poor (**A**). In that case, the oxygen interstitial defect O_i logically exhibits a low DFE. Moreover, one can notice that in such conditions, the calcium vacancy defect (V_{Ca}) is in close competition with O_i reaching similar concentration levels (Figure 7a). Furthermore, it should be mentioned that the Fermi level is pinned by V_{Ca} with an upper limit around 2 eV.

In the other extreme oxygen atmosphere (**B**), the oxygen vacancy is, as expected, strongly favored and the most likely defect (Figure 6b). in atmosphere (**C**), which corresponds to the center of the stability domain of the material, the oxygen vacancy recombines with a self-interstitial in the neighborhood of the Fermi level (Figure 6c). Furthermore, in that condition, the calcium vacancy is strongly favored compared to the other defects by several orders of magnitudes in concentration (Figure 7c).

In all cases, the tungsten vacancy is unlikely to be created due to very high formation enthalpy.

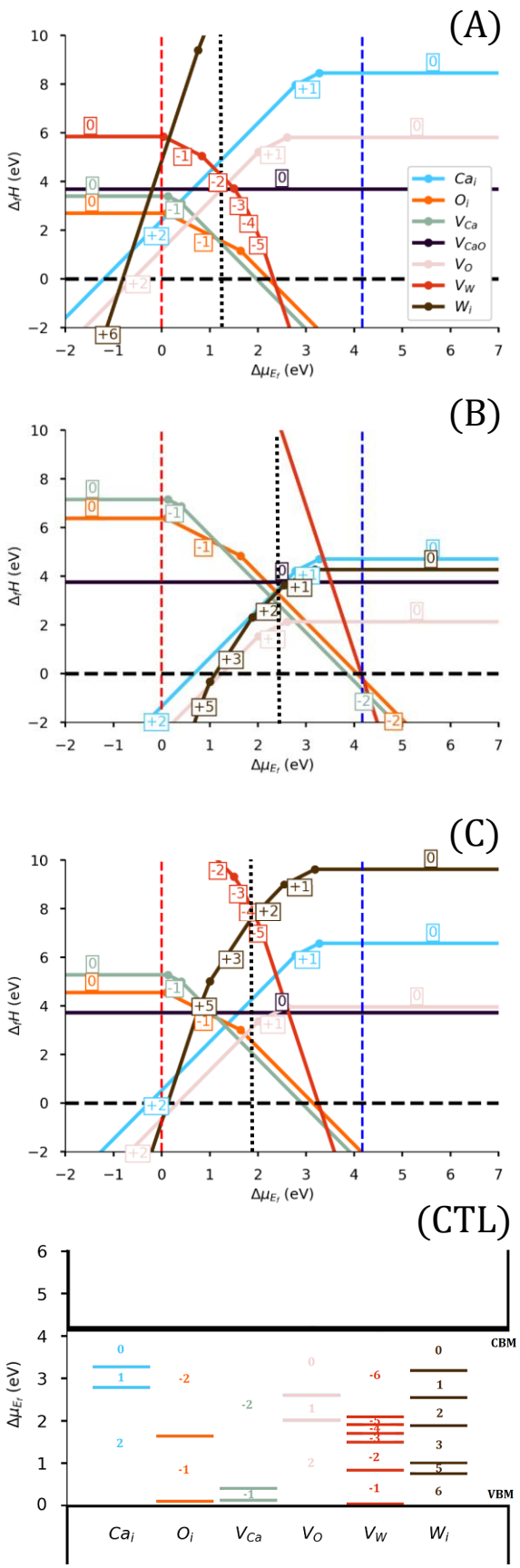

Figure 6: Intrinsic Defect Formation Energies of $CaWO_4$ in (**A**), (**B**) and (**C**) conditions, along with the charge transfer levels (CTL). For the DFE plots, the red, blue and black dashed lines correspond to the VBM, CBM and Fermi energy (at growth temperature= 800 K), respectively.

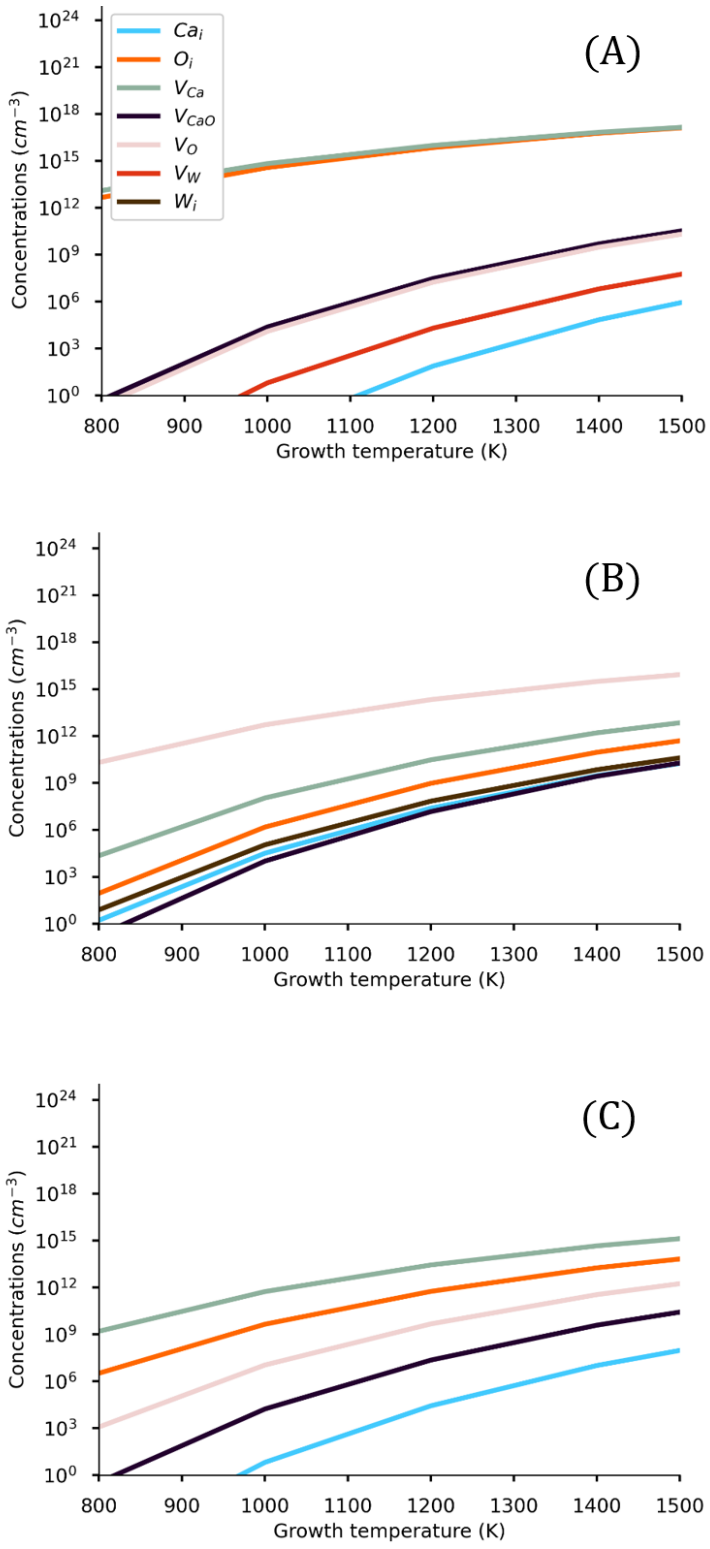

Figure 7: Intrinsic defect concentrations *vs.* growth temperature in different atmospheres. *For indication, the atomic concentration of Ca and W, and O in an ideal $CaWO_4$ material is ca. 1.27×10^{22} atoms/cm³ and ca. 5.09×10^{22} atoms/cm³ respectively.*

Excited state properties

To evaluate the luminescence properties, the excited state geometry of the solid was relaxed using the same CDFT procedure as in a previous work on ZrO_2.[56,57] Essentially, an electron was removed from the valence band maximum (VBM) of the ground state relaxed structure and transferred to the first available empty band. After relaxing the ions in the cell without symmetry constraints in this excited state configuration, the emission energy was calculated as the difference in energy between the excited state equilibrium geometry and the ground state energy at the excited state equilibrium energy level.[56]

According to the simulation, an electronic emission wavelength of 435 nm (2.85 eV) was found, which is really close to the observed one peaking at 420 nm (2.95 eV) and well below the maximum error bar allowed in DFT.

To gain a better understanding of the various processes involved, let us first examine the structural differences between the ground state of the excited state (relaxed configuration in an ideal and formal W-$5d^1$/O-$2p^5$ configuration) and the excited state of the ground state (configuration W-$5d^0$/O-$2p^6$ in the aforementioned W-$5d^1$/O-$2p^5$ configuration). The main modification is seen in the lengthening of four W-O bonds, which increase from 1.82 Å in the ground state to approximately 1.88 Å in the excited state for three of them, and almost 2.00 Å for the fourth. This lengthening in the excited state was expected due to the charge transfer occurring during the excitation process (see Figure 8). This structural modification indicates that the WO_4 tetrahedra are of high importance in the luminescence processes as proposed in a previous investigation.[2]

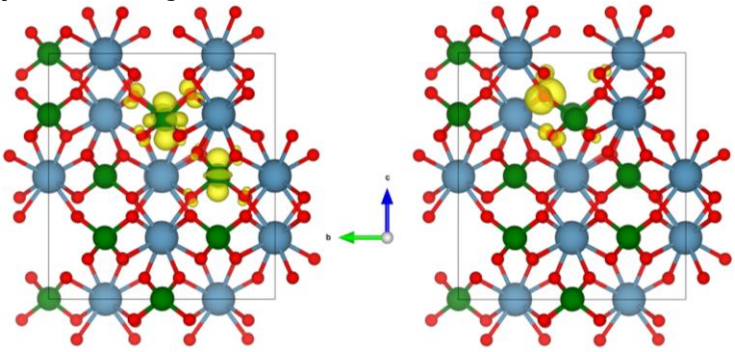

Figure 8: Localization of the charge density in the last occupied state in the excited (left) and ground states –using the relaxed excited state geometry- (right), respectively. The excited state is at the equilibrium, whereas the ground state is at the excited state structure but in the ground state electronic structure. This transfer corresponds to the de-excitation process. Ca, W and O correspond to the blue, green and red spheres, respectively.

In addition to accounting for electronic transitions, the vibrational contributions of the ground state supercell were included in order to simulate a vibrationally resolved spectrum. To do so, it was mandatory to perform a DFPT computation on the supercell's ground state to get the vibration using the VASP software. Figure 9 displays a visual comparison between the experimental and simulated spectra.[58] It is evident that, despite a slight overestimation of the emission wavelength, the agreement regarding the bandshape is very good. The deviation between the experimental and simulated spectra is approximately 0.15 eV, which falls within the acceptable range of errors in DFT, even using highly accurate methods at the molecular level.[59]

One way to circumvent this deviation would be to perform all the study using a global hybrid functional. However, it would increase the computational time by several order of magnitude due the size of the supercell. By aligning the simulated spectrum with the maximum of the experimental one, the coefficient of determination (R^2) was calculated to be 0.9940, further demonstrating the strength of our methodology.

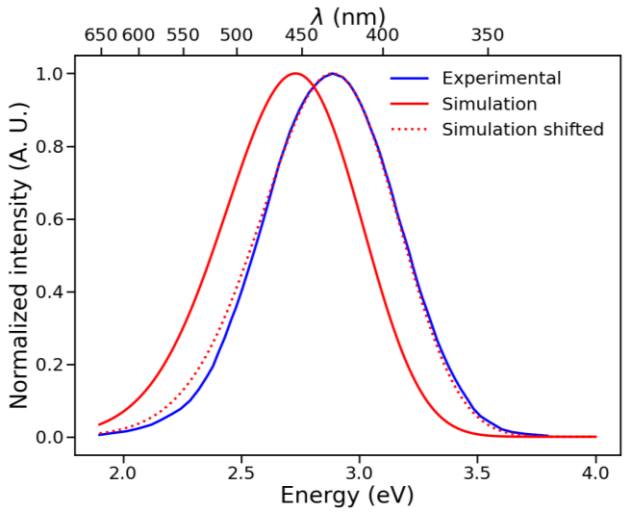

Figure 9: Simulated (red) vibrationally resolved and experimental[58] (blue) emission spectra of $CaWO_4$. The FWHM was set to 0.2 eV. The shifted spectrum is shifted to fit the experimental maximum.

Conclusion

In this study, ab initio computations were performed to investigate the structural, electronic, intrinsic defects, and luminescence properties of $CaWO_4$. The results were in good agreement with experimental values, demonstrating the accuracy of our approach. The Raman signatures were unambiguously assigned by comparing our simulation with experiment, the most common intrinsic defect were identified, the luminescence wavelength maximum was well simulated and we finally fully confirm the impact of the WO_4 tetrahedra in the luminescence process and the occupation of electronic orbitals in the excited state. Future studies could aim for greater accuracy by employing hybrid functionals, but this comes at a higher computational cost. Incorporating spin-orbit effects in all the investigated processes could also be of interest, but the current cost is prohibitively high. Finally, we intend to expand our methodologies to study other compounds of interest. Overall, this work provides valuable insights into the properties of $CaWO_4$ and can inform future research in the field.

Acknowledgements

CL, SJ and TC thank the ANR MoRDOR (ANR-20-CE08-0013). CL, SJ and TF thank the ANR PERSIST (ANR-18-CE08-0012).
This work was performed using HPC resources from GENCI-TGCC (Grants A010092471 and A0120913422), CCIPL (Centre de Calculs Intensifs des Pays de la Loire) and the IMN local cluster.

References

(1) Treadaway, M. J.; Powell, R. C. Luminescence of Calcium Tungstate Crystals. *J. Chem. Phys.* **1974**, *61* (10), 4003–4011. https://doi.org/10.1063/1.1681693.

(2) Grasser, R.; Scharmann, A.; Strack, K.-R. On the Intrinsic Nature of the Blue Luminescence in $CaWO_4$. *J. Lumin.* **1982**, *27*, 263–272. https://doi.org/10.1016/0022-2313(82)90004-7.

(3) Nagirnyi, V.; Feldbach, E.; Jönsson, L.; Kirm, M.; Lushchik, A.; Lushchik, Ch.; L. Nagornaya, L.; D. Ryzhikov, V.; Savikhin, F.; Svensson, G.; A. Tupitsina, I. Excitonic and Recombination Processes in $CaWO_4$ and $CdWO_4$ Scintillators under Synchrotron Irradiation. *Radiat. Meas.* **1998**, *29* (3), 247–250. https://doi.org/10.1016/S1350-4487(98)00017-1.

(4) Grasser, R.; Scharmann, A. Luminescent Sites in $CaWO_4$ and $CaWO_4$: Pb Crystals. *J. Lumin.* **1976**, *12–13*, 473–478. https://doi.org/10.1016/0022-2313(76)90125-3.

(5) Blasse, G.; Grabmaier, B. C. *Luminescent Materials*; Springer: Berlin, Heidelberg, 1994. https://doi.org/10.1007/978-3-642-79017-1.

(6) On a New Kind of Rays. *Nature* **1896**, *53* (1369), 274–276. https://doi.org/10.1038/053274b0.

(7) Sun, L.; Cao, M.; Wang, Y.; Sun, G.; Hu, C. The Synthesis and Photoluminescent Properties of Calcium Tungstate Nanocrystals. *J. Cryst. Growth* **2006**, *289* (1), 231–235. https://doi.org/10.1016/j.jcrysgro.2005.10.125.

(8) Mikhailik, V. B.; Bailiff, I. K.; Kraus, H.; Rodnyi, P. A.; Ninkovic, J. Two-Photon Excitation and Luminescence of a $CaWO_4$ Scintillator. *Radiat. Meas.* **2004**, *38* (4), 585–588. https://doi.org/10.1016/j.radmeas.2004.02.015.

(9) Baccaro, S.; Boháček, P.; Cecilia, A.; Laguta, V.; Montecchi, M.; Mihóková, E.; Nikl, M. Effect of La Doping on Calcium Tungstate ($CaWO_4$) Crystals Radiation Hardness. **2000**. https://doi.org/10.1002/1521-396X(200004)178:2<799::AID-PSSA799>3.0.CO;2-9.

(10) Gernand, M.; Görlich, P.; Hultzsch, R.; Kötitz, G.; Lüdke, W. Züchtung, spektroskopische Prüfung und Lasereigenschaften von Molybdat-und Wolframatkristallen mit Nd^{3+}-Dotierung. *Krist. Tech.* **1968**, *3* (2), 129–151. https://doi.org/10.1002/crat.19680030202.

(11) Orhan, E.; Anicete-Santos, M.; Maurera, M. A. M. A.; Pontes, F. M.; Souza, A. G.; Andrès, J.; Beltràn, A.; Varela, J. A.; Pizani, P. S.; Taft, C. A.; Longo, E. Towards an Insight on the Photoluminescence of Disordered $CaWO_4$ from a Joint Experimental and Theoretical Analysis. *J. Solid State Chem.* **2005**, *178* (4), 1284–1291. https://doi.org/10.1016/j.jssc.2004.12.038.

(12) Hu, W.; Tong, W.; Li, L.; Zheng, J.; Li, G. Cation Non-Stoichiometry in Multi-Component Oxide Nanoparticles by Solution Chemistry: A Case Study on $CaWO_4$ for Tailored Structural Properties. *Phys. Chem. Chem. Phys.* **2011**, *13* (24), 11634–11643. https://doi.org/10.1039/C0CP02153A.

(13) Su, Y.; Li, G.; Xue, Y.; Li, L. Tunable Physical Properties of $CaWO_4$ Nanocrystals via Particle Size Control. *J. Phys. Chem. C* **2007**, *111* (18), 6684–6689. https://doi.org/10.1021/jp068480p.

(14) Yekta, S.; Sadeghi, M.; Babanezhad, E. Synthesis of $CaWO_4$ Nanoparticles and Its Application for the Adsorption-Degradation of Organophosphorus Cyanophos. *J. Water Process Eng.* **2016**, *14*, 19–27. https://doi.org/10.1016/j.jwpe.2016.10.004.

(15) Ryu, E.-K.; Huh, Y.-D. Synthesis of $CaWO_4$ by a Microemulsion Method. *J. Korean Chem. Soc.* **2008**, *52*, 164–168. https://doi.org/10.5012/jkcs.2008.52.2.164.

(16) Wang, Y.; Ma, J.; Tao, J.; Zhu, X.; Zhou, J.; Zhao, Z.; Xie, L.; Tian, H. Synthesis of $CaWO_4$ Nanoparticles by a Molten Salt Method. *Mater. Lett.* **2006**, *60* (2), 291–293. https://doi.org/10.1016/j.matlet.2005.08.037.

(17) Vidya, S.; Solomon, S.; Thomas, J. K. Synthesis of Nanocrystalline $CaWO_4$ as Low-Temperature Co-Fired Ceramic Material: Processing, Structural and Physical Properties. *J. Electron. Mater.* **2013**, *42* (1), 129–137. https://doi.org/10.1007/s11664-012-2303-3.

(18) Cavalcante, L. S.; Longo, V. M.; Sczancoski, J. C.; Almeida, M. a. P.; Batista, A. A.; Varela, J. A.; Orlandi, M. O.; Longo, E.; Li, M. S. Electronic Structure, Growth Mechanism and Photoluminescence of $CaWO_4$ Crystals. *CrystEngComm* **2012**, *14* (3), 853–868. https://doi.org/10.1039/C1CE05977G.

(19) Yadav, P.; Dev Bhuyan, P.; Rout, S. K.; Sonvane, Y.; Gupta, S. K.; Sinha, E. Correlation between Experimental and Theoretical

Study of Scheelite and Wolframite-Type Tungstates. *Mater. Today Commun.* **2020**, *25*, 101417. https://doi.org/10.1016/j.mtcomm.2020.101417.

(20) Wang, S.; Gao, H.; Sun, G.; Li, Y.; Wang, Y.; Liu, H.; Chen, C.; Liang Yang. Structure Characterization, Optical and Photoluminescence Properties of Scheelite-Type $CaWO_4$ Nanophosphors: Effects of Calcination Temperature and Carbon Skeleton. *Opt. Mater.* **2020**, *99*, 109562. https://doi.org/10.1016/j.optmat.2019.109562.

(21) Spassky, D.; Mikhailin, V.; Nazarov, M.; Ahmad-Fauzi, M. N.; Zhbanov, A. Luminescence and Energy Transfer Mechanisms in $CaWO_4$ Single Crystals. *J. Lumin.* **2012**, *132* (10), 2753–2762. https://doi.org/10.1016/j.jlumin.2012.05.028.

(22) Lou, Z.; Cocivera, M. Cathodoluminescence of $CaWO_4$ and $SrWO_4$ Thin Films Prepared by Spray Pyrolysis. *Mater. Res. Bull.* **2002**, *37* (9), 1573–1582. https://doi.org/10.1016/S0025-5408(02)00851-6.

(23) Mikhailik, V. B.; Kraus, H.; Wahl, D.; Itoh, M.; Koike, M.; Bailiff, I. One- and Two-Photon Excited Luminescence and Band-Gap Assignment in $CaWO_4$. *Phys Rev B* **2004**, *69*. https://doi.org/10.1103/PhysRevB.69.205110.

(24) Mikhailik, V. B.; Kraus, H.; Miller, G.; Mykhaylyk, M.; Wahl, D. Luminescence of $CaWO_4$, $CaMoO_4$, and $ZnWO_4$ Scintillating Crystals under Different Excitations. *J. Appl. Phys. - J APPL PHYS* **2005**, *97*. https://doi.org/10.1063/1.1872198.

(25) Nagirnyi, V.; Kirm, M.; Kotlov, A.; Lushchik, A.; Jönsson, L. Separation of Excitonic and Electron-Hole Processes in Metal Tungstates. *J. Lumin.* **2003**, *102–103*, 597–603. https://doi.org/10.1016/S0022-2313(02)00596-3.

(26) Pankratov, V.; Millers, D.; Grigorjeva, L.; Chernov, S. Transient Optical Absorption and Luminescence in Calcium Tungstate Crystal. *Phys. Status Solidi B* **2001**, *225* (2), R9–R11. https://doi.org/10.1002/1521-3951(200106)225:2<R9::AID-PSSB99999>3.0.CO;2-Z.

(27) de Sousa, P. B.; Gouveia, A. F.; Sczancoski, J. C.; Nogueira, I. C.; Longo, E.; San-Miguel, M. A.; Cavalcante, L. S. Electronic Structure, Optical and Sonophotocatalytic Properties of Spindle-like $CaWO_4$ Microcrystals Synthesized by the Sonochemical Method. *J. Alloys Compd.* **2021**, *855*, 157377. https://doi.org/10.1016/j.jallcom.2020.157377.

(28) Williams, R. T.; Zhang, Y. C.; Abraham, Y.; Holzwarth, N. A. W. Electronic Structure of Pure and Defective $PbWO_4$, $CaWO_4$, and $CdWO_4$. 10.

(29) Basu, S.; Naidu, B. S.; Viswanadh, B.; Sudarsan, V.; Jha, S. N.; Bhattacharyya, D.; Vatsa, R. K. Nature of WO_4 Tetrahedra in Blue Light Emitting $CaWO_4$ Probed through the EXAFS Technique. *RSC Adv.* **2014**, *4* (30), 15606–15612. https://doi.org/10.1039/C3RA47619G.

(30) Arora, S. K.; Chudasama, B. Crystallization and Optical Properties of $CaWO_4$ and $SrWO_4$. *Cryst. Res. Technol.* **2006**, *41* (11), 1089–1095. https://doi.org/10.1002/crat.200610727.

(31) Lacomba-Perales, R.; Ruiz-Fuertes, J.; Errandonea, D.; Martínez-García, D.; Segura, A. Optical Absorption of Divalent Metal Tungstates: Correlation between the Band-Gap Energy and the Cation Ionic Radius. *EPL Europhys. Lett.* **2008**, *83* (3), 37002. https://doi.org/10.1209/0295-5075/83/37002.

(32) Maurera, M. A. M. A.; Souza, A. G.; Soledade, L. E. B.; Pontes, F. M.; Longo, E.; Leite, E. R.; Varela, J. A. Microstructural and Optical Characterization of $CaWO_4$ and $SrWO_4$ Thin Films Prepared by a Chemical Solution Method. *Mater. Lett.* **2004**, *58* (5), 727–732. https://doi.org/10.1016/j.matlet.2003.07.002.

(33) Saito, N.; Kudo, A.; Sakata, T. Synthesis of Tungstate Thin Films and Their Optical Properties. *Bull. Chem. Soc. Jpn.* **1996**, *69* (5), 1241–1245. https://doi.org/10.1246/bcsj.69.1241.

(34) Benmakhlouf, A.; Errandonea, D.; Bouhemadou, A.; Bentabet, A.; Maabed, S.; Bouchenafa, M.; Bin-Omran, S. Ab Initio Study of the Mechanical and Electronic Properties of Scheelite-Type XWO_4(X = Ca, Sr, Ba) Compounds. *Int. J. Mod. Phys. B* **2017**, *31* (12), 1750086. https://doi.org/10.1142/S0217979217500862.

(35) Zhang, Y.; Holzwarth, N. A. W.; Williams, R. T. Electronic Band Structures of the Scheelite Materials $CaMoO_4$, $CaWO_4$, $PbMoO_4$, and $PbWO_4$. *Phys. Rev. B* **1998**, *57* (20), 12738–12750. https://doi.org/10.1103/PhysRevB.57.12738.

(36) Kresse, G.; Hafner, J. Ab Initio Molecular Dynamics for Liquid Metals. *Phys. Rev. B* **1993**, *47* (1), 558–561. https://doi.org/10.1103/PhysRevB.47.558.

(37) Kresse, G.; Hafner, J. Ab Initio Molecular-Dynamics Simulation of the Liquid-Metal--Amorphous-Semiconductor Transition in Germanium. *Phys. Rev. B* **1994**, *49* (20), 14251–14269. https://doi.org/10.1103/PhysRevB.49.14251.

(38) Kresse, G.; Furthmüller, J. Efficiency of Ab-Initio Total Energy Calculations for Metals and Semiconductors Using a Plane-Wave Basis Set. *Comput. Mater. Sci.* **1996**, *6* (1), 15–50. https://doi.org/10.1016/0927-0256(96)00008-0.

(39) Kresse, G.; Furthmüller, J. Efficient Iterative Schemes for Ab Initio Total-Energy Calculations Using a Plane-Wave Basis Set. *Phys. Rev. B* **1996**, *54* (16), 11169–11186. https://doi.org/10.1103/PhysRevB.54.11169.

(40) Kaduk, B.; Kowalczyk, T.; Van Voorhis, T. Constrained Density Functional Theory. *Chem. Rev.* **2012**, *112* (1), 321–370. https://doi.org/10.1021/cr200148b.

(41) Moss, T. S. The Interpretation of the Properties of Indium Antimonide. *Proc. Phys. Soc. Sect. B* **1954**, *67* (10), 775–782. https://doi.org/10.1088/0370-1301/67/10/306.

(42) Burstein, E. Anomalous Optical Absorption Limit in InSb. *Phys. Rev.* **1954**, *93* (3), 632–633. https://doi.org/10.1103/PhysRev.93.632.

(43) Makov, G.; Payne, M. C. Periodic Boundary Conditions in Ab Initio Calculations. *Phys. Rev. B* **1995**, *51* (7), 4014–4022. https://doi.org/10.1103/PhysRevB.51.4014.

(44) Lany, S.; Zunger, A. Accurate Prediction of Defect Properties in Density Functional Supercell Calculations. *Model. Simul. Mater. Sci. Eng.* **2009**, *17*, 084002. https://doi.org/10.1088/0965-0393/17/8/084002.

(45) Komsa, H.-P.; Rantala, T. T.; Pasquarello, A. Finite-Size Supercell Correction Schemes for Charged Defect Calculations. *Phys. Rev. B* **2012**, *86* (4), 045112. https://doi.org/10.1103/PhysRevB.86.045112.

(46) Komsa, H.-P.; Rantala, T.; Pasquarello, A. Comparison between Various Finite-Size Supercell Correction Schemes for Charged Defect Calculations. *Phys. B Condens. Matter* **2012**, *407* (15), 3063–3067. https://doi.org/10.1016/j.physb.2011.08.028.

(47) Thorp, J. S.; Ammar, E. A. E. The Dielectric Constants of $CaWO_4$, Nd/$CaWO_4$ and Gd/$CaWO_4$. *J. Mater. Sci.* **1975**, *10* (6), 918–922. https://doi.org/10.1007/BF00823207.

(48) Brower, W. S.; Fang, P. H. Dielectric Constants of $PbWO_4$ and $CaWO_4$. *J. Appl. Phys.* **2004**, *38* (5), 2391–2392. https://doi.org/10.1063/1.1709895.

(49) Dovesi, R.; Erba, A.; Orlando, R.; Zicovich-Wilson, C. M.; Civalleri, B.; Maschio, L.; Rérat, M.; Casassa, S.; Baima, J.; Salustro, S.; Kirtman, B. Quantum-Mechanical Condensed Matter Simulations with CRYSTAL. *WIREs Comput. Mol. Sci.* **2018**, *8* (4), e1360. https://doi.org/10.1002/wcms.1360.

(50) Péan, E.; Vidal, J.; Jobic, S.; Latouche, C. Presentation of the PyDEF Post-Treatment Python Software to Compute Publishable Charts for Defect Energy Formation. **2017**. https://doi.org/10.1016/J.CPLETT.2017.01.001.

(51) Stoliaroff, A.; Jobic, S.; Latouche, C. PyDEF 2.0: An Easy to Use Post-Treatment Software for Publishable Charts Featuring a Graphical User Interface. *J. Comput. Chem.* **2018**, *39* (26), 2251–2261. https://doi.org/10.1002/jcc.25543.

(52) Kuz'micheva, G.; Kaurova, I. Peculiar Structural Effects in Pure and Doped Functional Single Crystals of Complex Compositions. *Molecules* **2020**, *25*, 2451. https://doi.org/10.3390/molecules25102451.

(53) Schira, R.; Latouche, C. DFT and Hybrid-DFT Calculations on the Electronic Properties of Vanadate Materials: Theory Meets Experiments. *New J. Chem.* **2020**, *44* (27), 11602–11607. https://doi.org/10.1039/D0NJ02316G.

(54) Bond, W. L. Measurement of the Refractive Indices of Several Crystals. *J. Appl. Phys.* **1965**, *36* (5), 1674–1677. https://doi.org/10.1063/1.1703106.

(55) Kraus, H.; Mikhailik, V. B.; Ramachers, Y.; Day, D.; Hutton, K. B.; Telfer, J. Feasibility Study of a $ZnWO_4$ Scintillator for Exploiting Materials Signature in Cryogenic WIMP Dark Matter Searches. *Phys. Lett. B* **2005**, *610* (1), 37–44. https://doi.org/10.1016/j.physletb.2005.01.095.

(56) Lafargue-Dit-Hauret, W.; Schira, R.; Latouche, C.; Jobic, S. Theoretical Calculations Meet Experiment to Explain the Luminescence Properties and the Presence of Defects in M-ZrO_2. *Chem. Mater.* **2021**, *33* (8), 2984–2992. https://doi.org/10.1021/acs.chemmater.1c00590.

(57) Cavignac, T.; Jobic, S.; Latouche, C. Modeling Luminescence Spectrum of $BaZrO_3$:Ti Including Vibronic Coupling from First Principles Calculations. *J. Chem. Theory Comput.* **2022**, *18* (12), 7714–7721. https://doi.org/10.1021/acs.jctc.2c00949.

(58) Yakovyna, V.; Zhydachevskii', Ya.; Mikhailik, V. B.; Solskii, I.; Sugak, D.; Vakiv, M. Effect of Thermo-Chemical Treatments on the Luminescence and Scintillation Properties of CaWO4. *Opt. Mater.* **2008**, *30* (10), 1630–1634. https://doi.org/10.1016/j.optmat.2007.11.003.

(59) Schira, R.; Latouche, C. DFT vs. TDDFT vs. TDA to Simulate Phosphorescence Spectra of Pt- and Ir-Based Complexes. *Dalton Trans.* **2021**, *50* (2), 746–753. https://doi.org/10.1039/d0dt03614e.